

Simulating radiation and kinetic processes in relativistic plasmas

R. Belmont^{1*}, J. Malzac¹, A. Marcowith²

¹ Centre d'Etude Spatiale des Rayonnements (OMP; UPS; CNRS), 9 avenue du Colonel Roche, BP44346, 31028, Toulouse Cedex 4, France

² Laboratoire de Physique Théorique et d'Astroparticules, IN2P3/CNRS, Université MontpellierII, CC 70, place Eugène Bataillon, F-34095 Montpellier Cedex 5, France

Received — / Accepted —

ABSTRACT

Context. Modelling the emission properties of compact high energy sources such as X-ray binaries, AGN or γ -ray bursts represents a complex problem. Contributions of numerous processes participate non linearly to produce the observed spectra: particle-particle, particle-photon and particle-wave interactions. In the past decades, numerical simulations have been widely used to address the key properties of the high energy plasmas present in these sources.

Aims. This article presents a code that has been designed to investigate these questions. It includes most of the relevant processes needed to simulate the emission of high energy sources.

Methods. This code solves the time-dependent kinetic equations for homogeneous, isotropic distributions of photons, electrons and positrons. No assumption is made on the shape of these distributions. Have been included so far: synchrotron self-absorbed radiation, Compton scattering, pair production/annihilation, e-e and e-p Coulomb collisions and some prescriptions for additional particle heating and acceleration.

Results. We also present comparisons with earlier works and some examples to illustrate the code computational capacities. Previous results are reproduced qualitatively but some differences are often found in the details of the particle distribution. As a first application of the code, we investigate acceleration by second order Fermi-like processes and we find that the energy threshold for acceleration has a crucial influence on the particle distribution and the emitted spectrum.

Key words. Radiation mechanisms: general - Plasmas - methods: numerical - Galaxies: active - X-rays: binaries, galaxies - Gamma rays: bursts

Introduction

High energy sources such as X-ray binaries, active galactic nuclei (AGN hereafter) or γ -ray bursts exhibit spectra extending to very high energy. This radiation must originate from a plasma in which a significant fraction of the particles have relativistic energies. Understanding the properties of these hot plasmas has been a challenge for almost half a century and is still an issue in the modelling of X- and γ -ray sources.

Among the many processes at work, there are particle-particle interactions such as Coulomb collisions, particle-photon interactions such as Compton scattering, synchrotron radiation or pair production/annihilation and particle-wave interactions that lead to particle acceleration...However the way they add or compete is highly non-linear and the involved cross sections are quite complex. Moreover investigating a large parameter space is required and in spite of important breakthroughs, these plasmas are still poorly understood. Analytical studies have provided very interesting qualitative results under approximations, but a more general approach based on numerical simulations is required in order to explain the details and complexity of contemporary observations. The first detailed investigations were analytical attempts to model the Compton scattering in thermal plasmas of fixed temperature (e.g.

Bisnovatyi-Kogan et al. 1971; Sunyaev & Titarchuk 1980; Guilbert 1981; Zdziarski 1985; Guilbert 1986). In parallel, some of these results were confirmed by Monte-Carlo simulations (e.g. Pozdnyakov et al. 1983; Gorecki & Wilczewski 1984). Further work was then made on the additional role of pair production and annihilation in thermal plasmas whose temperatures were determined self-consistently. Again, this was investigated both analytically (Svensson 1982b, 1983; Guilbert & Stepney 1985; Kusunose 1987) and numerically (Zdziarski 1984, 1985). These works constituted significant advances since they explicitly accounted for the back reaction of the radiation field on the plasma temperature. However they were limited to thermal distributions of particles whereas large evidences were found for strongly non-thermal populations in many sources. For instance, spectra of blazars or radio loud AGN have been shown to be shaped at least by the synchrotron self-Compton emission of purely non-thermal electrons (e.g. Ghisellini et al. 1998b). At these high energies, accelerated particles cool on very short time scales before they can be thermalized by two body collisions for instance. The balance between this cooling and acceleration typically leads to non-thermal distributions. Acceleration processes are still poorly understood. A simple way to account for particle acceleration consists in injecting particles at high energy. Although it does not reproduce exactly the involved physics, this prescription has been widely used in the literature and has led to interest-

* e-mail: belmont@cesr.fr

ing results (most of the references cited here). Large effort has also been spent on more precise modelling of acceleration mechanisms, but then the radiation field is treated crudely (Li et al. 1996; Dermer et al. 1996; Li & Miller 1997; Katarzyński et al. 2006b).

With the increasing number of considered processes and the increasing precision of their description, numerics has become a prime method of investigation. Even so, a full treatment of the problem accounting for the coupled evolution of inhomogeneous, anisotropic distributions of leptons and photons, both in momentum and position spaces, seems to be still out of reach of present days computers power. Numerical simulations of high energy plasmas have been performed mainly following three different approaches which all make trade-offs between the various aspects of the problem.

First, the Monte-Carlo technique (Pozdnyakov et al. 1977; Stern et al. 1995) allows one to follow particles and photons in space, time and energy as they undergo mutual interactions. In that sense it solves the full radiative transfer problem and thus takes explicitly geometrical effects into account. At present days the MC method is probably the best way to deal with fully 3-dimensional problems. However, this detailed procedure is time consuming, particularly when modelling the very fast dynamics of the non-thermal electron population in momentum space (Malzac & Jourdain 2000) and when synchrotron self absorption effects are important (see discussion in Stern et al. (1995)). For this reason, the Monte-Carlo methods have been, so far, essentially applied to pure Maxwellian plasmas and/or steady state problems in 3D geometry.

Another method that accounts correctly for the geometry, consists in solving numerically the exact radiation transfer equation for given geometries and particles distributions (Poutanen & Svensson 1996). This method is much faster than Monte Carlo simulations which makes it easier to compare with the data. Its drawbacks are that it is much less versatile than Monte-Carlo methods and that the kinetic equations for particles is not solved. It allows one to take into account the back reaction of the radiation field on the particle distribution only under the assumption of a Maxwellian plasma (in which case the plasma temperature may be adjusted according to energy balance). The applicability of this method is also limited to the resolution of steady state problems.

The third approach, that we will adopt in this paper, gives up the detailed description of the geometry in order to concentrate on the kinetic effects. It consists in solving the local kinetic equations for the distributions of particles and photons. For the sake of fast computing, radiative transfer is usually modelled using a simple photon escape probability formalism assuming isotropic photon and particle distributions. This method can be applied to very different, possibly time-dependent, problems as long as geometry does not play a crucial role¹. Within the limits of the 1-zone approximation, it is more efficient than other methods and allows for efficient data fitting.

¹ For problems in which geometry is important, radiative transfer can in principle be accounted for by coupling such a kinetic code with a radiation transfer solver or a Monte-Carlo code (as done by Böttcher & Liang (2001)), although computing time may then become a serious issue.

The first detailed investigations of high energy plasmas with this technique concentrated on thermal pair plasmas (Fabian et al. 1986; Ghisellini 1987). More precise modelling was then proposed where the particle distributions are decomposed as the sum of a thermal low-energy pool and an arbitrary high energy tail (Lightman & Zdziarski 1987; Svensson 1987; Coppi 1992; Zdziarski et al. 1993; Ghisellini et al. 1993; Li et al. 1996). The latter models have been the most used when fitting and interpreting the data. They however do not describe the possible deviation from a Maxwellian distribution at low energy, nor they address explicitly any thermalization process. Only the most recent numerical works deal with fully arbitrary distributions of particles. Ghisellini et al. (1998a) concentrated on the role of synchrotron self-absorbed radiation in AGN. They confirmed previous analytical work (Ghisellini et al. 1988) by showing that exchange of energy between particles by the mean of synchrotron photons can be an efficient thermalization process in magnetized sources. These simulations however focused on this peculiar interaction and other processes were only considered in crude approximations, particularly Compton radiation, or not considered at all. Nayakshin & Melia (1998) investigated the thermalization of arbitrary distributions by two body particle interactions and the heating by high energy protons. The additional role of synchrotron radiation was however not considered. The most complete numerical treatment of high energy plasmas was probably developed in the context of γ -ray bursts (Pe’er & Waxman 2005). Our code is partly similar but differs as the authors did not considered any particle stochastic acceleration in their calculation neither the effect of Coulomb losses.

The code presented here solves simultaneously the time dependent equations for isotropic, arbitrary photons, electrons and positrons distributions. These populations are evolved under effect of self-absorbed cyclo-synchrotron radiation, Compton scattering, pair production/annihilation, e-e and e-p Coulomb collisions and additional particle acceleration and heating. Each process is described in an accurate way with minimal approximations by using for most of them the exact cross sections. For instance, formulae for the synchrotron emission and absorption are used that are valid from the sub-relativistic to the ultra-relativistic regime. This numerical strategy allows one to investigate many different astrophysical situations arising in various high energy sources.

The structure of this paper is as follows. Sec. 1 provides a description of the microphysics involved in the code. Then, in Sec. 2, we explicitly present the numerical techniques. Finally, in Sec. 3 the code is critically tested against previous published results, providing an overview of its capabilities.

1. Radiation and kinetic processes

In this section, we describe the various processes that have been included into the code so far. Here are the general notations used in this paper. The particle energy is described alternatively by their relativistic Lorentz factor $\gamma = E/m_e c^2$, by their adimensional momentum $p = \mathcal{P}/m_e c = \sqrt{\gamma^2 - 1}$ or by their beta parameter $\beta = p/\gamma$, where m_e is the electron mass and c is the speed of light. Similarly, the photon energies are described by their frequencies ν or by $\omega = h\nu/m_e c^2$. The particle and photon

populations are described by their angle-averaged distribution functions $N_{e^\pm} = \frac{\partial \mathcal{N}_{e^\pm}}{\partial^3 x \partial p}$ and $N_\nu = \frac{\partial \mathcal{N}_\nu}{\partial^3 x \partial \nu}$, where $\partial \mathcal{N}_{e^\pm}$ and $\partial \mathcal{N}_\nu$ are the number of electrons, positrons and photons per unit volume $\partial^3 x$ and per unit momentum ∂p or frequency $\partial \nu$. Also, for seek of simplicity, the total lepton distribution is used: $N_e = N_{e^-} + N_{e^+}$. Finally, R is the typical length scale of the emission region. Since we consider an homogeneous medium, most of the processes are actually scale free, meaning that most quantities are simply proportional to R , R^2 or R^3 . For those quantities, R only determines the overall normalization factor. For instance the total luminosity of unmagnetized sources scales as R^3 , but there is no reference scale in the problem. The only process explicitly involving a reference length scale is the synchrotron self-absorption since it is independently determined by both the magnetic intensity and the total magnetic energy of the source which is directly related to the source size for a given magnetic intensity (see hereafter).

1.1. Self-absorbed Synchrotron Radiation

The cyclo-synchrotron radiation process is produced by charged particles gyrating along magnetic field lines. It is one of the most important processes in astrophysics and is invoked to explain the radio emission of many magnetized sources such as supernova remnants, pulsar wind nebulae, AGN, X-ray binaries, γ -ray bursts... In particular, it produces soft photons that can be up scattered by Compton scattering producing the well known double humped synchrotron self-compton spectra used to model the emission of blazars or radio loud AGN for example. The reverse process, cyclo-synchrotron absorption, is less known, although it very efficient at low energy. Besides explaining some observed spectra, cyclo-synchrotron emission and absorption both influence the involved particles by cooling and heating them respectively. As discussed later on such interactions can thermalize high energy particles (the so called *synchrotron boiler*, Ghisellini et al. 1988).

Here following the main assumption of the code, we assume isotropy of the radiation field and the particle pitch angle. These are good approximations when the magnetic field is very tangled. The cyclo-synchrotron emission and absorption are characterized by the emissivity spectrum $j_s(p, \nu)$ ($\text{erg s}^{-1} \text{Hz}^{-1}$) of one single particle of momentum p and the cross section $\sigma_s(p, \nu)$ (cm^2). Both quantities are related to each other by the formula (Le Roux 1961; Ghisellini et al. 1988; Ghisellini & Svensson 1991)²:

$$\sigma_s(p, \nu) = \frac{1}{4\pi} \frac{1}{2m_e \nu^2} \frac{1}{p^2} \partial_p [p \gamma j_s(p, \nu)] \quad (1)$$

where m_e is the electron mass. The emissivity and cross-section depend on the magnetic field whose intensity is characterized by the *magnetic compactness* (Ghisellini et al. 1988):

$$l_B = \frac{\sigma_T R B^2}{m_e c^2 8\pi} \quad (2)$$

As mentioned earlier, the synchrotron self-absorption explicitly depends on the source size. Although the overall

normalization of the emissivity and absorption is only proportional to a combination of the magnetic field intensity and the source size (namely l_B), their shape depends on the cyclotron frequency $\nu_B = eB/2\pi m_e c$ that depends only on the magnetic field intensity. For a given magnetic compactness parameter, simulations of sources with different sizes correspond to cases with different magnetic field intensities and thus produce different observed spectra.

In uniform systems, the time evolution of the mean intensity integrated over solid angles $I_\nu = h\nu c N_\nu$ ($\text{erg s}^{-1} \text{Hz}^{-1} \text{cm}^{-2}$) is described by the equation:

$$\partial_t I_\nu / c = \mu_\nu - \kappa_\nu I_\nu \quad (3)$$

with

$$\mu_\nu = \int N_e j_s(p, \nu) dp \quad (\text{erg cm}^{-3} \text{s}^{-1} \text{Hz}^{-1}), \quad (4)$$

$$\kappa_\nu = \int N_e \sigma_s(p, \nu) dp \quad (\text{cm}^{-1}). \quad (5)$$

Note that this equation is different from the one often used in previous works (for example Ghisellini et al. 1988, 1998a). The latter have mostly concentrated on the steady state properties of magnetized sources and did not include this time dependence. In order to account for photon escape and the non-absorbed part of the observed spectra, a finite size domain is assumed in these papers and the space equation $\partial_x I_\nu = \mu_\nu - \kappa_\nu I_\nu$ is solved for uniform emissivity μ_s and absorption κ_s on a typical length scale R giving the synchrotron self-absorbed radiation: $I_\nu = \mu/\kappa(1 - e^{-\kappa R})$. This corresponds to an approximated way to deal with the space dependence of the simulated system since it implies a non-uniform synchrotron radiation whose feedback on the lepton equation would need to be incorporated in a fully space-dependent model to be relevant. Moreover such a solution holds when only synchrotron self-absorption is involved. Other processes such as Compton scattering or pair production/annihilation would also contribute to the emissivity μ and absorption κ in some way and in such description it is not clear how the synchrotron interaction couples to others in the global equation for the radiation field. Here we consider a homogeneous (or averaged) radiation field which, associated with the photons escape probability (see discussion in section 1.6) represents an another approximated way to deal crudely with the geometry. However, this method solves the exact time-dependent equation and the synchrotron emission is consistently added to other emission processes.

Simultaneously, the equation for the time evolution of the lepton populations is (McCray 1969; Ghisellini et al. 1988):

$$\partial_t N_{e^\pm} = \partial_p \left(\frac{\gamma}{p} A_e^s N_{e^\pm} \right) + \frac{1}{2} \partial_p \left[\frac{\gamma}{p} \partial_p \left(\frac{\gamma}{p} D_e^s N_{e^\pm} \right) \right] \quad (6)$$

where the γ/p factors result from the choice of p as a variable instead of γ and

$$A_e^s = \frac{1}{m_e c^2} \int (j_s - \sigma_s I_\nu) d\nu \quad (\text{s}^{-1}), \quad (7)$$

$$D_e^s = \frac{1}{4\pi} \frac{1}{m_e^2 c^2} \int \frac{j_s I_\nu}{\nu^2} d\nu \quad (\text{s}^{-1}). \quad (8)$$

Equation 6 can be written in many different ways that are analytically equivalent. The one we use (Eq. 6-8), associated with a specific numerical scheme to estimate derivatives, allows very good numerical accuracy. In particular,

² The term $1/4\pi$ in Eq. 1 and 8 comes from the average over the solid angle

the energy conservation can easily be satisfied to machine precision when particles and the photon field exchange energy, since $dE_e/dt = mc^2 \int \gamma \partial_p [A_e N_e] dp = - \iint (j_s - \sigma_s I_\nu) N_e dp d\nu = - \int (\mu_s - \kappa_s I_\nu) d\nu = -dE_\nu/dt$.

There is no exact analytical expression for pitch angle averaged- and photon direction integrated- emissivity and absorption that are valid in all regimes. The exact values result from numerical integrations that are very time consuming and hard to perform, especially for low energy particles when the emission is dominated by a few narrow harmonics. However, a number of approximations have been proposed that are valid in some regimes (e.g. Marcowith & Malzac 2003). We use a combination of two approximations. For sub-relativistic particles, we use the formula for j_s first proposed by Ghisellini et al. (1998a) and recently corrected by Katarzyński et al. (2006a) to 1- better match the relativistic spectrum, 2- better describe the spectrum near the minimal frequency. This approximation is less accurate for very low energy particles (typically $\beta \lesssim 0.1$). However, for most astrophysical cases, the emission is mainly produced by energetic particles, so that this regime has only little influence on the total particles distribution and radiation field. Numerical experiments have confirmed that the choice of j_s and σ_s at low energy has negligible effect. For the relativistic regime, we use the well known synchrotron power spectrum integrated over an isotropic distribution of pitch angles (Crusius & Schlickeiser 1986; Ghisellini et al. 1988). Note that we make similar correction to this formula so that it better matches the sub-relativistic regime. The transition between both regimes is made by performing an exponential threshold/cut-off for the formulas at $\gamma = 2$. The formulae for σ_s are computed analytically from j_s with Eq. 1 and implemented into the code.

1.2. Compton Scattering

Compton scattering is a well known interaction between leptons and photons. Most of the previous studies assumes thermal distributions of particles. In such case, only the temperature and total number of particles are computed. This assumption allows fast computation with simple formulae but misses out the physics of non-thermal particles. Here we use exact analytical expressions for unpolarized radiation and arbitrary distribution of isotropic particles and photons.

1.2.1. Basic equations

The effect of Compton scattering can be described by the sum of individual encounters over the entire distributions. The scattering of isotropic photons of energy $h\nu_0 = \omega_0 m_e c^2$ off isotropic particles of energy $E_0 = \gamma_0 m_e c^2$ is fully characterized by the resulting distribution of scattered photons $\sigma_c(p_0, \nu_0 \rightarrow \nu)$. This differential Klein-Nishina cross section has been computed by several authors (Jones 1968; Brinkmann 1984; Nagirner & Poutanen 1994). The numerical evaluation of these analytical expressions can be difficult especially for low or high energy particles and photons. Here we use an expression based on the formulae by Jones (1968) and modified to overcome numerical accuracy issues (Belmont 2008).

The exact time evolution of the full particle and photon distributions are described by the following equations:

$$\partial_t N_{e^\pm}(p) = \iint N_{e^\pm}(p_0) N_\nu(\nu_0) c \sigma_c(p_0, \nu_0 \rightarrow \nu(p)) dp_0 d\nu_0 - N_{e^\pm}(p) \int N_\nu(\nu_0) c \sigma_0^c(\nu_0, p) d\nu_0, \quad (9)$$

$$\partial_t N_\nu(\nu) = \iint N_e(p_0) N_\nu(\nu_0) c \sigma_c(p_0, \nu_0 \rightarrow \nu) dp_0 d\nu_0 - N_\nu(\nu) \int N_e(p_0) c \sigma_0^c(\nu, p_0) dp_0 \quad (10)$$

where the photon frequency $\nu(p)$ is defined by the energy conservation during one scattering event : $h(\nu(p) - \nu_0) + (\gamma - \gamma_0) m_e c^2 = 0$. For each distribution, the first integral gives the number density of scattered particles/photons that end up with a given energy after one single scattering and the second one is the probability that particles/photons of this energy are scattered off to some other energy. This is what we call the *integral approach*. As discussed hereafter, the numerical computation of this integral suffers from accuracy issues because of discretization.

In the small angle scattering limit, that is to say when the scattered photons (or particle) have an energy similar to that of the incoming ones, a *Fokker-Planck approximation* can be used (FP hereafter). In this case, a second order series expansion of the exact equations gives the FP evolution equations for the different species:

$$\partial_t N_\nu(\nu) = \partial_\omega [A_\nu^c N_\nu] + \frac{1}{2} \partial_\omega^2 [D_\nu^c N_\nu], \quad (11)$$

$$\partial_t N_{e^\pm}(p) = \partial_p \left(\frac{\gamma}{p} A_e^c N_{e^\pm} \right) + \frac{1}{2} \partial_p \left[\frac{\gamma}{p} \partial_p \left(\frac{\gamma}{p} D_e^c N_{e^\pm} \right) \right] \quad (12)$$

with

$$A_\nu^c = - \int N_e c \sigma_1^c(p, \nu) dp, \quad D_\nu^c = \int N_e c \sigma_2^c(p, \nu) dp, \quad (13)$$

$$A_e^c = \int N_\nu c \sigma_1^c(p, \nu) d\nu, \quad D_e^c = \int N_\nu c \sigma_2^c(p, \nu) d\nu \quad (14)$$

and where we have introduced the first 3 moments of the scattered photon distribution:

$$\sigma_0^c(p_0, \nu_0) = \int \sigma_c(p_0, \nu_0 \rightarrow \nu) d\nu, \quad (15)$$

$$\sigma_1^c(p_0, \nu_0) = \int (\omega - \omega_0) \sigma_c(p_0, \nu_0 \rightarrow \nu) d\nu, \quad (16)$$

$$\sigma_2^c(p_0, \nu_0) = \int (\omega - \omega_0)^2 \sigma_c(p_0, \nu_0 \rightarrow \nu) d\nu \quad (17)$$

the total cross section, the mean photon energy, and the dispersion respectively.

This approximation allows much quicker computation since, once the first moments have been tabulated, only single integrals are required whereas the exact computation requires double integrals. However, the Fokker-Planck approach used for the evolution of particles and photons distributions is only valid in regions of the incident energy space (ν_0, p_0) for which the relative energy exchange in one scattering is small: $\Delta [h\nu(p_0, \nu_0)] / (m_e c^2 \gamma(p_0)) \ll 1$ and $\Delta \nu(p_0, \nu_0) / \nu_0 \ll 1$ respectively. These conditions are investigated in more detail in Belmont (2008).

1.2.2. Numerical strategy

Contrary to the Fokker-Planck approximation, the integral approach is analytically exact. However, when used to compute numerically the evolution, it leads to some numerical issues directly related to the use of non-linear grids (Nayakshin & Melia 1998).

With logarithmic grids, the energy bin size is larger at high energy. When, for example, low energy photons are scattered off high energy particles, their relative energy gain is large, and such photons are numerically scattered from low energy bins to higher energy bins. During this interaction, the particles only lose a small fraction of their energy. If the energy bin size is too large, these particles remain in their original bin and numerically, they do not lose any energy. Thus, the energy balance is not exactly satisfied and the error can propagate and become large when the density of low energy photons is also large. Although less relevant in most astrophysical situations a symmetrical problem appears when high energy photons scatter off low energy particles.

This numerical issue is not present in regions of the incident energy space (p_0, ν_0) for which the scattered distributions are much wider than the energy bin size: $\Delta\nu(p_0, \nu_0)/\delta\nu(\nu_0) \gg 1$ and $\Delta[h\nu(p_0, \nu_0)]/(m_e c^2 \delta\gamma(p_0)) \gg 1$ for the evolution of the photons and particles distributions respectively. Once ranges and a resolution for the photon and particle energy grids have been chosen, these conditions set the region where the integral approach is valid. Fortunately, the regions where the integral and the Fokker-Planck approaches are valid are partly complementary. The code thus combines the two approaches:

- For the particles evolution:

In the integral approach, the integration over the photon distribution in Eq. 9 is only performed above a given photon energy $\nu_c(p_0)$ that depends on the incident particle energy, whereas the integrals in Eq. 14 are done up to ν_c in the Fokker-Planck approach. The total time evolution is then the sum of both contributions: $\partial_t N_{e^\pm} = (\partial_t N_{e^\pm})_{\text{FP}} + (\partial_t N_{e^\pm})_{\text{Integral}}$.

- For the photons evolution:

A similar combination is used with the definition of a critical particle momentum $p_c(\nu_0)$ under which the FP approach is used and above which the integral approach is used.

The validity domains for both calculations may be disjoined if the number of energy bins per decade is too small. If so, the computation may lack of accuracy. However, it usually affects only small regions of the grids where there are few particles and photons, leading to very small errors. We find empirically that, by combining the two approaches, an energy resolution of typically 10 energy bins per decade gives errors that are smaller than other truncation errors.

1.3. Pair production/annihilation

As for Compton scattering, we describe the pair production and annihilation in the case of isotropic distributions of particles and photons. Single photon-photon pair production and pair annihilation events are characterized respectively by the differential cross sections: $\sigma^p(\nu_1, \nu_2 \rightarrow p)$ that corresponds to the pair (i.e. electrons or positrons) momentum spectrum resulting from the recombination of photons of frequencies ν_1 and ν_2 , and $\sigma_a(p_-, p_+ \rightarrow \nu)$ that corre-

sponds to the emission spectrum resulting from the annihilation of one electron of momentum p_- and one positron of momentum p_+ . Then, the evolution of the distributions is described by:

$$\partial_t N_{e^\pm}(p) = \iint N_\nu(\nu_1) N_\nu(\nu_2) c \sigma_p(\nu_1, \nu_2 \rightarrow p) d\nu_1 d\nu_2 - N_{e^\pm}(p) \int N_{e^\mp}(p') \sigma_0^a(p, p') dp', \quad (18)$$

$$\partial_t N_\nu(\nu) = \iint N_{e^-}(p_-) N_{e^+}(p_+) c \sigma_a(p_-, p_+ \rightarrow \nu) dp_- dp_+ - N_\nu(\nu) \int N_\nu(\nu') \sigma_0^p(\nu, \nu') d\nu' \quad (19)$$

where, as for Compton scattering, the zeroth moment of the annihilation spectrum $\sigma_0^a(p_-, p_+) = 1/2 \int \sigma_a(p_-, p_+ \rightarrow \nu) d\nu$ and of the pair-produced distribution $\sigma_0^p(\nu_1, \nu_2) = 2 \int \sigma_p(\nu_1, \nu_2 \rightarrow p) dp$ have been used³. The analytical expressions for photon-photon pair production and pair annihilation correspond to Eq. (24-29) of Boettcher & Schlickeiser (1997) and Eq. (23,33,55-58) of Svensson (1982a) respectively.

Contrary to Compton scattering, there is no numerical issue in computing directly the integral over the particle and photon distributions, even for low resolution grids.

1.4. Coulomb scattering

Two kinds of Coulomb-type interactions are considered: scattering of leptons off other leptons and scattering of leptons off protons. When the particles are not too energetic, e-e collisions tend to thermalize the pair distributions. In most astrophysical situations, protons are assumed to have a large temperature, so that e-p collisions tend to heat the lepton populations. Both kinds of interactions are described by the Boltzmann collision integral. Computing numerically this integral is very challenging, mainly because the Coulomb cross section diverges when the energy exchange becomes too small. We rather make the approximation of small angle scattering, which leads to simple Fokker-Planck equations. As has been already discussed in the literature, the contribution of large angle scattering is negligible (Dermer & Liang 1989; Nayakshin & Melia 1998).

1.4.1. Moeller and Bhabha e-e scattering

The FP coefficients (A^{e-e} and D^{e-e}) for Moeller $e^\pm - e^\mp$ and Bhabha $e^\pm - e^\pm$ scattering are very similar. The relative difference is typically of the order of $\sim 1/\ln \Lambda$ where the Coulomb logarithm $\ln \Lambda$ is large (Dermer & Liang 1989). Neglecting such terms, the FP coefficients are computed from the following integrations over the mirror distributions:

$$A_{e^\pm}^{e-e}(p_\pm) = \int N_{e^\mp}(p_\mp) a_e(p_-, p_+) dp_\mp, \quad (20)$$

$$D_{e^\pm}^{e-e}(p_\pm) = \int N_{e^\mp}(p_\mp) d_e(p_-, p_+) dp_\mp. \quad (21)$$

The specific coefficients a_e and d_e were first given by Nayakshin & Melia (1998) (Eq. 24 and 35 respectively).

³ The 1/2 and 2 factors result from the fact that one pair annihilation produces 2 photons and one photon-photon annihilation produces 2 leptons.

The equation for d however contains typos that were corrected by Eq. 6 of Blasi (2000).

1.4.2. Coulomb e-p scattering

In many astrophysical situations, protons can not cool by radiation and are thought to have temperatures much larger than those of electrons. In such cases, Coulomb collisions with leptons tend to heat the latter. As for the e-e collisions, the FP coefficients (A^{e-p} and D^{e-p}) for e-p Coulomb scattering are computed from integrals over the proton distribution:

$$A_{e\pm}^{e-p}(p_e) = \int N_p(p_p) a_p(p_e, p_p) dp_p, \quad (22)$$

$$D_{e\pm}^{e-p}(p_e) = \int N_p(p_p) d_p(p_e, p_p) dp_p \quad (23)$$

where a_p and d_p are derived from Eq. (45) to (48) of Nayakshin & Melia (1998). The code could calculate the exact proton distribution as it does for electrons and positrons. However, it would add a fourth kinetic equation and require more computational time. We rather use a thermal proton distribution. Depending on the physical situation being modelled, the proton temperature can be set to a constant at the beginning of the simulations or evolved with time to provide a constant electron heating. The latter case mimics the proton equilibrium between the cooling by collisions with electrons and some external heating mechanism, the rate of which is set by a heating compactness parameter:

$$l_c = \frac{4\pi}{3} \frac{R^2 \sigma_T}{c} \int -\eta A_{e\pm}^{e-p} N_e dp. \quad (24)$$

1.5. Particle and photon injection

The code also allows for injection of particles into the system. This can represent a real injection from an outer source (e.g. particles from the standard disk into an ADAF). Injection of high energy particles is commonly used to mimic particle acceleration processes. Any distribution $\dot{N}_{e\pm}^{\text{inj}}$ can be injected at each time step. Thermal, Gaussian, power-law and mono-energetic injections have already been included into the code. The injection of particles is controlled by the particle injection compactness⁴:

$$l_{e\pm} = \frac{\dot{E}_{\text{inj}}}{m_e c^3 R / \sigma_T} = \frac{R^2 \sigma_T}{c} \frac{4\pi}{3} \int \gamma \dot{N}_{e\pm}^{\text{inj}} dp. \quad (25)$$

Similarly, the code allows for photons injection that can account for seed photons from the cold accretion disk in X-ray binaries for example. The injection of photons is controlled by the parameter:

$$l_\nu = \frac{L_{\text{inj}}}{m_e c^3 R / \sigma_T} = \frac{R^2 \sigma_T}{c} \frac{4\pi}{3} \int \frac{h\nu}{m_e c^2} \dot{N}_\nu^{\text{inj}} d\nu. \quad (26)$$

⁴ Note that some authors rather use the kinetic energy to define the compactness parameter: $l_{e\pm} = 4\pi R^2 \sigma_T / 3c \int (\gamma - 1) \dot{N}_{e\pm}^{\text{inj}} dp$.

1.6. Particle and photon losses: geometry of the source

Generally speaking, photons and particles can also be lost from the system. The precise way they escape depends on the detailed geometry of the simulated source, which goes beyond the scope of such a 1-zone kinetic code. Although the losses must occur at the boundaries of the simulated plasma we use a standard method and we consider that all photons (or particles) have the same averaged probability p_ν^{esc} (or $p_{e\pm}^{\text{esc}}$) to escape. We assume a spherical geometry and use probability laws that describe such a geometry approximately. Then, the total luminosity of the source at each frequency is:

$$L_\nu = \frac{4\pi R^3}{3} h\nu P_\nu^{\text{esc}} N_\nu \quad (27)$$

The code allows for fully trapped pairs in very magnetized systems (no loss) and for freely escaping pairs (with an escape probability proportional to their velocity: $p_{e\pm}^{\text{esc}} = \beta c/R$). Other escape laws can be defined and implemented easily.

The photon escape is more debatable. The photon dynamics is strongly affected by Compton scattering. Basically, high energy photons do not scatter and can escape freely whereas, when the optical depth is large, low energy photons can scatter to a point where they are trapped into the system. The exact way they escape, depending on their energy, strongly involves geometrical effects. In the code we use the escape rate r_ν^{esc} (or escape probability defined as $p_\nu^{\text{esc}} = r_\nu^{\text{esc}} \times R/c$) derived by Lightman & Zdziarski (1987):

$$r_\nu^{\text{esc}} = 1/T_\nu^{\text{esc}} = \frac{c/R}{1 + \tau(\omega)f(\omega)/3} \quad (28)$$

where T_ν^{esc} is the averaged escape time and

$$\tau(\omega = h\nu/m_e c^2) = R\sigma_T \int N_e \frac{\sigma_0^c(\nu, p)}{\sigma_T} dp \quad (29)$$

is the Compton interaction probability of photons (of frequency ν) with the lepton distributions and

$$f(\omega = h\nu/m_e c^2) = \begin{cases} 1 & \text{for } \omega \leq 0.1 \\ (1 - \omega)/0.9 & \text{for } 0.1 < \omega \leq 1 \\ 0 & \text{for } \omega \geq 1 \end{cases} \quad (30)$$

is a relativistic factor correcting for the fact that forward collisions are less efficient in trapping the photons.

The choice for the escape probability is quite important and different laws can lead to substantially different results⁵. Although it has been shown that this escape probability reproduces quite well the results of Monte-Carlo simulations in a spherical geometry (Lightman et al. 1987; Lightman & Zdziarski 1987), the conclusions of Stern et al. (1995) suggest that it may be slightly underestimated. Since the escaping luminosity must equal the injected power in steady state, a smaller escape probability implies a stronger radiation field inside the source. The consequences on the

⁵ For instance, when comparing his results with those of Lightman & Zdziarski (1987), Coppi (1992) attributed the difference to different descriptions of the microphysics, whereas from several simulations, we think most of it directly results from a different choice for the escape rate: he used $(R/c)/(1 + \tau(\omega)f(\omega))$ instead of Eq.28.

shape of the photon and lepton distributions then become significant only when pair production and annihilation are very efficient (typically at high optical depths). Fig. 1 shows spectra in such cases where the deviation from the Monte-Carlo simulations become significant. Other escape probabilities have been proposed (e.g. Stern et al. 1995) that may better match the results from MC simulations in some specific regimes, but none have been shown to be fully consistent with MC simulations. The use of an escape probability to mimic geometrical effects is obviously the main limitation of our code. However significant deviations only appear in optically thick plasmas when steep gradients in temperature and intensity appear, whereas jets and cor- nae in XRB and AGN are rather optically thin media, the largest optical depths observed being $\tau \approx 2 - 3$. Moreover the precise geometry of sources is not known, so that having an accurate description for the exact escape probability in one peculiar geometry is not necessarily relevant.

1.7. Additional particle heating/acceleration

Particle heating and acceleration are probably some of the most mysterious problems in high energy sources. Observations show evidence for hot plasmas or high energy tails in the particle distributions, but little is known about the exact mechanisms that generate such populations. Most of previous works do not address this problem directly. Instead, non-thermal high energy high energy particles are injected in the system with an arbitrary (usually power law) distribution. This ad hoc injection assumes an instantaneous acceleration of particles. It does not take into account the fact that particle acceleration has to compete with other cooling processes. Another simple approach, often used to account for lepton heating consists in assuming that power is provided by some unspecified process to the supposedly thermal distribution of electrons. These prescriptions for particle acceleration and heating are implemented in the code. However, in addition, we also attempted to follow a more physical approach by implementing two additional specific mechanisms for heating and acceleration, namely Coulomb heating and second order Fermi acceleration.

- e-p Coulomb-like heating:

As has already been discussed, collisions with hot protons can heat the pair distributions. The way the exact interaction is included in the code is described in section 1.4.2. When the Thomson optical depth is less than unity, such heating is known to become very inefficient and other processes must be at work that are not understood. A possible prescription to account for this additional heating is to mimic the heating by thermal protons but with an enhanced efficiency (Nayakshin & Melia 1998). Although it is not aimed to describe any precised microphysics, this heating prescription consistently estimates both FP coefficients: the heating rate and its related diffusion coefficient. For this heating prescription, the temperature and total number of protons are set to satisfy the initial neutrality. Then the usual cooling and diffusion coefficients $A_{e^\pm}^{e-p}$ (Eq. 22) and $D_{e^\pm}^{e-p}$ (Eq. 23) are multiplied by an efficiency factor η . This efficiency is computed at each time step so that the total heating is controlled by a constant heating compactness parameter.

- 2nd order Fermi-like acceleration:

This kind of acceleration could arise for example as the

result of the interaction between the electron with wave turbulence. Diffusion of particles in the momentum space is then described by the general equation:

$$\frac{\partial f}{\partial t} = \frac{1}{p^2} \frac{\partial}{\partial p} \left[p^2 D^{\text{diff}} \frac{\partial f}{\partial p} \right] \quad (31)$$

where $f(p)$ is the phase-space density. When going to an equation on N_{e^\pm} it yields a Fokker-Planck equation with the two coefficients:

$$A_{e^\pm}^{\text{acc}} = -\frac{1}{p\gamma} \partial_\gamma \left(\frac{p^3}{\gamma} D^{\text{diff}} \right), \quad (32)$$

$$D_{e^\pm}^{\text{acc}} = 2 \frac{p^2}{\gamma^2} D^{\text{diff}}. \quad (33)$$

Here we assume a Fermi-like process for particles having an energy above some minimal energy and we use $D^{\text{diff}} = p^2 e^{-(p_c/p)^a} / 2t_{\text{acc}}$ where p_c is the threshold momentum, a is the threshold width (we use typically $a = 3$), and t_{acc} is the typical acceleration time of the particles (Katarzyński et al. 2006b). Then the FP coefficients are:

$$A_{e^\pm}^{\text{acc}} = -\frac{1}{2t_{\text{acc}}} \frac{p^2}{\gamma^3} \left(5 + 4p^2 + a\gamma^2 \left(\frac{p_c}{p} \right)^a \right) e^{-(p_c/p)^a}, \quad (34)$$

$$D_{e^\pm}^{\text{acc}} = \frac{1}{t_{\text{acc}}} \frac{p^4}{\gamma^2} e^{-(p_c/p)^a}. \quad (35)$$

The exact values for the acceleration time and the cut off frequency depend on the microphysics and the turbulent properties of the plasma that are poorly known. Here we rather set the total energy injected into accelerated particles by defining a constant compactness parameter:

$$l_{\text{acc}} = \frac{4\pi}{3} \frac{R^2 \sigma_T}{c} \int -A_{e^\pm}^{\text{acc}} N_e dp \quad (36)$$

and we compute the corresponding acceleration time at each time step.

1.8. Bremsstrahlung emission

The Bremsstrahlung process has several contributions to the system evolution: it produces additional soft photons that can then be up-scattered by high energy particles, it cools down emitting, high energy particles and, in the absorbed part, it heats low energy particles. In arbitrary plasmas there are three different contributions: lepton-proton ($e-p$), electron-electron or positron-positron ($e-e$), and electron-positron ($e^- - e^+$) Bremsstrahlung.

Electron-proton self-absorbed Bremsstrahlung is included in the code. Proton are assumed to have non-relativistic temperature and to be at rest in the plasma frame. Then, the emission results from the motion of leptons in the external electro-static potential of protons. The situation is formally the same as in the case of synchrotron emission which results from the motion of leptons an external magnetic field and a similar formalism can be used (Le Roux 1960; Ghisellini & Svensson 1991). The exact interaction cross-section σ_{ep}^0 valid for all lepton energies (Heitler 1954; Jauch & Rohrlich 1976) is used to compute the emissivity spectrum j_{ep} ($\text{erg s}^{-1} \text{Hz}^{-1}$) of individual electrons and the absorption cross section σ_{ep} (cm^2):

$$j_{\text{ep}}(p, \nu) = h\nu \beta c \sigma_{\text{ep}}^0(p, \nu) N_p^{\text{tot}} \quad (37)$$

$$\sigma_{\text{ep}}(p, \nu) = \frac{1}{4\pi} \frac{1}{2m_e \nu^2} \frac{1}{p^2} \partial_p [p\gamma j_{\text{ep}}(p, \nu)] \quad (38)$$

where N_p^{tot} is the proton density and $\beta = v/c$ is the lepton velocity and σ_{ep} is evaluated numerically. Approximations for the total loss rate and the spectrum emitted by a thermal plasma are recovered by integrating j_{ep} over a thermal distribution of leptons. Then, the evolution equations for particles and photons are derived exactly as in the case of synchrotron emission (Eq. 3-8).

Electron-proton Bremsstrahlung is the dominant contribution in low energy, e-p plasmas. In low energy, pair plasmas the $e^+ - e^-$ process dominates whereas at high temperatures the major contribution comes from $e - e$ Bremsstrahlung. Differential cross sections for $e - e$ and $e^- - e^+$ Bremsstrahlung found in various regimes either in the rest frame of one of the leptons or in the centre of mass of the two interacting particles (Heitler 1954; Alexanian 1968; Haug 1975, 1985). However there is no formula in the frame of the plasma for the cross section integrated over all directions of the emitted photon, and simpler thermal approximations are often not relevant since the cross section typically increases with the particle energy and non thermal emission of high energy particles often dominates the overall Bremsstrahlung emission. In principle, these difficulties could be overcome numerically.

However in many astrophysical cases Bremsstrahlung emission is not significant. For plasmas in thermal equilibrium, simple approximations have been proposed for the cooling rates, which allows for comparison with other processes (e.g. Gould 1980; Stepney & Guilbert 1983). It is found that the bremsstrahlung cooling dominates over pair annihilation cooling and Coulomb relaxation only for highly relativistic temperatures: $k_B T \gtrsim 1$ MeV (Svensson 1982b; Stepney 1983, respectively). Also, by integrating the synchrotron and Compton cooling rates over a hot thermal distribution of particles ($k_B T = 1$ MeV) in the radiation energy density U_ν , we find that for plasmas with optical depth of the order of unity Bremsstrahlung emission dominates only when $R\sigma_T U_\nu / m_e c^2 + l_B \lesssim 4 \times 10^{-3}$, that is for unmagnetized, photon-starved plasmas. For these compactness parameters, only hotter plasmas have a significant Bremsstrahlung contribution, however for astrophysical sources such high temperatures are not realistic since pair production/annihilation tend to prevent temperatures above a few hundreds keV (Svensson 1984). Similarly it has been shown that non thermal particles mostly emit synchrotron radiation even for weak magnetic fields (Wardziński & Zdziarski 2000; Coppi 1992).

For these reasons, $e - e$ and $e^- - e^+$ Bremsstrahlung has not been included in the code yet and the modelling of unmagnetized, highly relativistic plasmas with a weak radiation field is postponed to future work.

2. Numerical methods

Finally, including all these processes, the total physical system is described by the following set of 3 integro-differential equations:

$$\partial_t N_\nu = S_\nu - P_\nu N_\nu + \partial_\omega [A_\nu N_\nu] + \frac{1}{2} \partial_{\omega^2} [D_\nu N_\nu] , \quad (39)$$

$$\begin{aligned} \partial_t N_{e^\pm} = & S_{e^\pm} - P_{e^\pm} N_{e^\pm} + \partial_p [\gamma/p A_{e^\pm} N_{e^\pm}] \\ & + \frac{1}{2} \partial_p \left[\frac{\gamma}{p} \partial_p \left(\frac{\gamma}{p} D_{e^\pm} N_{e^\pm} \right) \right] . \quad (40) \end{aligned}$$

Here the source terms $S_\nu(t, \nu, N_\nu, N_{e^-}, N_{e^+})$ and $S_{e^\pm}(t, p, N_\nu, N_{e^-}, N_{e^+})$ combine the contributions of injection, Compton scattering (treated in the integral approach), annihilation/production and synchrotron emission:

$$\begin{aligned} S_\nu = & \dot{N}_\nu^{\text{inj}}(t, \nu) \\ & + \int_0^\infty d\nu_0 \int_{p_c(\nu_0)}^\infty dp_0 N_e(p_0) N_\nu(\nu_0) c \sigma^c(p_0, \nu_0; \nu) \\ & + \iint_0^\infty N_{e^-}(p_-) N_{e^+}(p_+) c \sigma_a(p_-, p_+; \nu) dp_- dp_+ \\ & + \frac{1}{h\nu} \int N_e(j_s + j_{ep}) dp , \quad (41) \end{aligned}$$

$$\begin{aligned} S_{e^\pm} = & \dot{N}_{e^\pm}^{\text{inj}}(t, p) \\ & + \int_0^\infty dp_0 \int_{\nu_c(p_0)}^\infty d\nu_0 N_e(p_0) N_\nu(\nu_0) c \sigma^c(p_0, \nu_0; \nu(p)) \\ & + \iint_0^\infty N_\nu(\nu_1) N_\nu(\nu_2) c \sigma_p(\nu_1, \nu_2; p) d\nu_1 d\nu_2 . \quad (42) \end{aligned}$$

The loss terms $P_\nu(t, \nu, N_\nu, N_{e^-}, N_{e^+})$ and $P_{e^\pm}(t, p, N_\nu, N_{e^\mp})$ also combine contributions from escape, Compton scattering, pair production/annihilation and synchrotron absorption:

$$\begin{aligned} P_\nu = & p_\nu^{\text{esc}}(\nu, N_{e^-}, N_{e^+}) + \int_{p_c(\nu)}^\infty N_e(p) c \sigma_0^c(p, \nu) dp \\ & + \int N_\nu(\nu') c \sigma_0^p(\nu, \nu') d\nu' + \int N_e c (\sigma_s + \sigma_{ep}) dp , \quad (43) \end{aligned}$$

$$\begin{aligned} P_{e^\pm} = & p_{e^\pm}^{\text{esc}}(p) + \int_{\nu_c(p_0)}^\infty N_\nu(\nu) c \sigma_0^c(p, \nu) d\nu \\ & + \int N_{e^\mp}(p') c \sigma_0^a(p, p') dp' . \quad (44) \end{aligned}$$

Finally, the total Fokker-Planck coefficients are the sums of the individual coefficients defined for each process:

$$A_\nu = - \int_0^{p_c(\nu)} N_e(p) c \sigma_1^c(\nu, p) dp , \quad (45)$$

$$D_\nu = \int_0^{p_c(\nu)} N_e(p) c \sigma_2^c(\nu, p) dp \quad (46)$$

and

$$\begin{aligned} A_{e^\pm} = & \frac{1}{m_e c^2} \int ((j_s + j_{ep}) - c(\sigma_s + \sigma_{ep}) h\nu N_\nu) d\nu \\ & + \int_0^{\nu_c(p)} N_\nu(\nu) c \sigma_1^c(\nu, p) d\nu \\ & + \int N_{e^\mp}(p') a_e(p, p') dp' + \int N_p(p') a_p(p, p') dp' \\ & + A_{e^\pm}^{\text{e-p}} + A_{e^\pm}^{\text{acc}} , \quad (47) \end{aligned}$$

$$\begin{aligned} D_{e^\pm} = & \frac{1}{4\pi m_e^2 c} \int \frac{(j_s + j_{ep}) N_\nu}{\nu} d\nu \\ & + \int_0^{\nu_c(p)} N_\nu(\nu) c \sigma_2^c(\nu, p) d\nu \\ & + \int N_{e^\mp}(p') d_e(p, p') dp' + \int N_p(p') d_p(p, p') dp' \\ & + D_{e^\pm}^{\text{e-p}} + D_{e^\pm}^{\text{acc}} . \quad (48) \end{aligned}$$

In this section, we describe the numerical strategy used to solve these equations.

2.1. Tables

Solving Eq. 39 and 40 with the mentioned physical processes makes abundant use of the many cross-sections ($j_s, \sigma_s, j_{ep}, \sigma_{ep}, \sigma_c, \sigma_0^c, \sigma_1^c, \sigma_2^c, \sigma_a, \sigma_0^a, \sigma_p, \sigma_0^p, a_e, d_e, a_p, d_p$). The Compton differential cross-section $\sigma^c(\nu_0, p_0 \rightarrow \nu)$ is a three entry table that typically contains over tens of millions elements. And so are the differential cross-sections for pair production/annihilation. These coefficients are computed once at the beginning and stored into tables. This allows faster computation but the memory requirements can become large when the grid resolution increases. For instance resolutions higher than 256 points per grid require more than 100 Mo RAM to store only one of these tables, which can be limiting with some desktop computers.

2.2. Boundaries

The total set of equations to solve involves an integro-differential system. To account for particles and photons that have energies outside of the grids (very low- or very high energy particles/photons), specific conditions must be set at the grid boundaries ω_{\min} , ω_{\max} , p_{\min} and p_{\max} . For the differential Fokker-Planck part of the equation which corresponds to a *local* operator, the boundary conditions only set values for the *ghost* bins just behind the boundaries and are used to define the derivative at the boundaries. For the integral part, they include the physics of all particles and photons outside the grids. We have chosen to use wall-type boundary conditions. These conditions do not allow for particles/photons going in and out of the grids and conserve their total number exactly. In the Fokker-Planck part, it corresponds to a zero flux condition. For the integral part, a specific derivation of the differential cross section is made: the total probability that particles/photons are scattered or produced outside the grids is summed and added to the probability that they are scattered or produced at the last bin of the relevant boundary. As a result, all particles/photons remain in the grids. Such conditions are bound to be artificial and to bring spurious effects at the boundaries. However, as far as most of the particles/photons have energies inside the grids, such effects remain small.

For example, although the total number of particles/photons is conserved, the no flux condition for the FP part of the equations introduces at the boundaries a small energy flux that can be evaluated easily. Namely, the energy losses are $dE_\omega/dt = m_e c^2 [D_\omega N_\omega]_{\omega_{\min}}^{\omega_{\max}}$ and $dE_{e^\pm}/dt = m_e c^2 [\gamma/p D_{e^\pm} N_{e^\pm}]_{p_{\min}}^{p_{\max}}$ for the photons and the leptons respectively. When the grid is not large enough, this effect can introduce large errors but by choosing the boundaries far from the bulk, the distributions N_ω and N_{e^\pm} vanish and the losses are negligible.

2.3. Numerical solver

Solving the time dependent problem is challenging for many reasons.

First the problem involves many different energy and time scales spanning over many orders of magnitude. This

implies subtracting very large terms or multiplying very small ones by very large ones, which can lead to numerical accuracy issues.

This also implies to deal with very short times scales. For instance, when low energy photons are scattered by high energy particles, they gain much energy instantaneously, which requires the use of very small time steps. If the problem was linear and differential, the maximal time step to guaranty the convergence and stability of an explicit scheme would be set by the Courant condition (Courant, Friedrichs & Lewy 1928). In that particular case, our simple scheme for the equation on photons would be stable if: $\delta t < \min \{ \delta\omega/A_\nu; 2(\delta\omega)^2/D_\nu \}$ where $\delta\omega$ is the bin size and the minimum is computed over the entire grid. Similarly, a condition depending on the momentum bins would be set for the stability of the equation for particles. When logarithmic grids are used, the time step is set to a very small value by the small bins at the very low energy part of the grids. Here, the equation are much more complicated, so that there is no mathematical justification for using the Courant condition. However, the main idea remains: when the grids go down to very low energy, the time step required to make an explicit scheme stable quickly becomes too small to follow the evolution on the dynamical time scale R/c .

In such cases, implicit scheme are more efficient, since they are always stable. Implicit schemes are easy to implement and very efficient only for local, linear problems. When the problem is linear, the solver only inverts a matrix. For local problems, i.e. differential ones, such a matrix is sparse and quickly inverted. Here however, the problem is highly non local. For example, the integral approach of the Compton scattering describes events where photons in some energy bin can be scattered out to some very distant bin in one single interaction. As a result, the evolution of the photon distribution at some energy is governed not only by the neighbour bins, but by the entire grid. The corresponding matrix is dense and its inversion becomes more time consuming. In addition, the problem is highly non-linear, so that there is no *exact* implicit solution for such problem.

Considering the previous remarks we implemented a semi-implicit scheme. Having the other distributions fixed, we solve the equation for the distribution N of one species (photons, electrons or positrons) in the following way:

$$\frac{N^{n+1} - N^n}{\delta t} = S^n - P^n N^{n+1} + \partial_x [A^n N^{n+1}] + \frac{1}{2} \partial_x^2 [D^n N^{n+1}] \quad (49)$$

where the exponents n and $n+1$ indicate the distributions and coefficients at two consecutive time steps. The scheme is not fully implicit but the equations for N_ν^{n+1} , $N_{e^-}^{n+1}$ and $N_{e^+}^{n+1}$ can be solved easily by inverting a simple multi-diagonal matrix. This scheme as such only conserves the number of particles/photons and their energy to the truncations of the time scheme. As as been explained earlier, using grids spanning over many orders of magnitude introduces accuracy issues. These issues become severe when number and energy are only conserved to truncation errors. For that reason, the code iterates the 3 equations represented by Eq. 49 at each time step until the conservation laws are satisfied to some given precision.

Two spatial schemes have been implemented to solve Eq. 49: The upwind Chang-Cooper method (Chang & Cooper 1970) and a more straight forward method we have developed. The former is only first order accurate in space but was shown to have the best numerical properties for solving Fokker-Planck equations with a few choices of *constant* coefficients (Park & Petrosian 1996). Compared to higher order schemes, it is more diffusive, i.e. more stable but less accurate. Here accuracy is very important, so that we rather use a second order accurate scheme to estimate the derivatives⁶. This scheme is based on the use of two energy grids for each distribution (namely the centers and the faces of the bins) and derivatives are computed as follows: $(\partial_x f)_i = (f_{i+1/2} - f_{i-1/2})/(dx_i)$ and $(\partial_x^2 f)_i = ((f_{i+1} - f_i)/dx_{i+1/2} - (f_i - f_{i-1})/dx_{i-1/2})/dx_i$. All quantities at the bin boundaries are computed by linear interpolation: $f_{i+1/2} = (f_i + f_{i+1})/2$ except the $(p/\gamma)_{i+1/2}$ factor in Eq. 12 for particles which is computed separately as $(p_i + p_{i+1})/(\gamma_i + \gamma_{i+1})$ to ensure accurate energy conservation. This simple centered scheme happens to better conserve the total number of particles and photons as well as the total energy (although less stable). All examples presented here were performed with the latter scheme.

2.4. Computation time

Tests and applications shown in this work have been performed with medium energy resolution: typically $n_\nu = 128 - 256$ and $n_p = 256$, i.e more than 20 bins per decade in particle momentum and more than 10 bins per decade in photon frequency. Compared to former codes (Lightman & Zdziarski 1987; Coppi 1992) that assume that low energy particles are purely thermal, our code typically solves the equations on twice more bins in particle momentum. In addition, as has been presented, it makes very few approximations and only when they are valid. The code is therefore slower than some previous codes. All results presented here were obtained on desktop computers with 1GHz processors and 512 MB RAM. Runs last typically from a few seconds to one hour, the most time consuming step being the computation of the multiple integrals of the Compton and pair production/annihilation cross sections over the distributions.

3. Tests and applications

In this section we present a few first applications of the code to check its capabilities and illustrate the problems that can be addressed. Most of the examples presented here consist in comparisons with previous works although we also address a few more issues such as the threshold for particle acceleration.

⁶ The scheme is second order accurate only when the grid is linear. Using a logarithmic grid as we do here actually reduces the accuracy. Nevertheless, numerical experiments with the code have shown that this scheme is more accurate than the Chang-Cooper method.

3.1. Model with external soft photons

Large effort has already been spent on the steady state solutions of unmagnetized sources. Here we only repeat some of the known results to check the code computational capacities. As a first case, we reproduce the results of Fig. 1 in Coppi (1992) with parameters typical of AGN. This case is modelled by injecting mono-energetic $e^+ - e^-$ pairs at $\gamma = 10^3$ and soft photons as a black body of temperature $k_B T = 1.07 \times 10^{-5} m_e c^2$. In this unmagnetized source, the length scale is unimportant. All effects are included except additional particle acceleration and e-p Coulomb scattering. Fig. (1) shows spectra obtained with the code and comparisons with previous work. Some outputs are also pre-

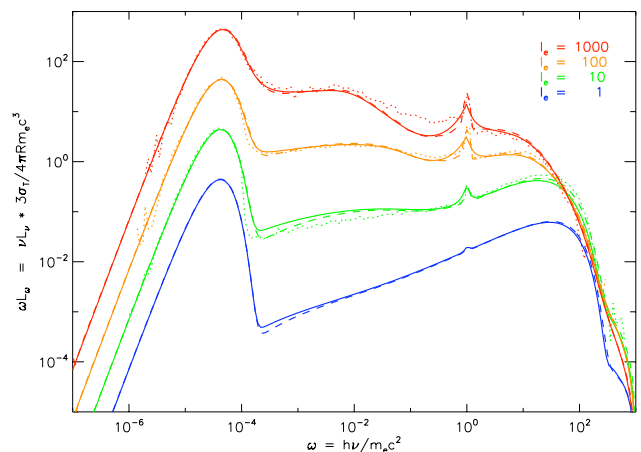


Fig. 1. Photon spectra for models with external soft photons ($l_e = l_{e^-} + l_{e^+} = 1, 10, 100, 1000$ from lower to higher curve and $l_\nu = 2.5l_e$). Solid lines: this work, dashed lines: results with the EQPAIR code and dotted lines: results from Monte Carlo simulation in spherical geometry (Stern et al. 1995). The spectra from EQPAIR were normalized to match the other ones. For simpler comparison the escape probability $p_\nu^{\text{esc}} = 1/(1 + \tau f)$ of Coppi (1992) is used for this figure.

sented in table 1. The temperature of this table was computed using Eq. (2.8) in Coppi (1992) only on the thermal part of the particle distribution. The results are fully consistent with both published results and results computed with the latest version of the public EQPAIR code. The major deviations appear at the annihilation line for large optical depths and luminosities ($l_e = 100$ and 1000).

When $\tau_e/(l_e + l_\nu) \gtrsim 1$, effects of pair annihilation and Coulomb scattering become strong. We investigated this regime by reproducing the results presented in Fig. 2 of Coppi (1992). This simulation has the same input parameters as the previous one, except that particles are injected with a power law distribution ($\gamma_{\text{min}} = 1.4$, $\gamma_{\text{max}} = 10^3$, $\Gamma = 2.4$, $l_e = 1$) and $l_\nu = 0.03$. The particle distribution and photon spectrum for such a case are plotted on Fig. 2. The corresponding outputs parameters are listed in table 2. Again, a good agreement is observed. It is particularly striking for the particle distribution, confirming that in this peculiar case, the approximations made by Coppi (1992)

l_e	work	PY ₃	τ_e	θ_3	l_X/l_e	α_{2-10}
1	Coppi92	1.7	0.047	7.9	—	0.637
	EQPAIR	—	0.078	12.6	0.0582	0.614
	This work	1.70	0.059	8.64	0.0611	0.633
10	Coppi92	23	0.502	5.7	—	0.863
	EQPAIR	—	0.508	8.27	2.70	0.854
	This work	22.6	0.548	4.50	3.00	0.901
10 ²	Coppi92	87	3.34	2.2	—	0.979
	EQPAIR	—	3.17	2.56	63.9	0.996
	This work	80	3.22	1.96	61.9	1.02
10 ³	Coppi92	120	12.4	0.62	—	1.42
	EQPAIR	—	11.95	0.567	644	1.39
	This work	112	12.01	0.44	628	1.41

Table 1. Models with external soft photons: comparison with previous results. PY₃ is 10³ times the pair yield defined in Coppi (1992). $\tau_e = R\sigma_T \int (N_{e^-} + N_{e^+}) dp$ is the total Thomson optical depth. $\theta_3 = 10^3 \times k_B T / m_e c^2$ is the temperature of the thermal part of the distribution. l_X/l_e is the ratio of the X-ray luminosity in the 2-10 keV band to the injection compactness parameter. α_{2-10} is the spectral index in the same energy band.

	PY ₃	τ_e	θ_3	l_X/l_e	α_{2-10}
Coppi92	3.54	0.644	306	0.077*	0.726
This work	3.27	0.624	273	0.0733	0.717

Table 2. Output parameters for $l_e = 1$ and $l_\nu = 0.03$. Same as table 1. *Note that the luminosity obtained by Coppi (1992) was multiplied by 10 to correct what we think is a typo.

were valid. The only difference arises at high energy in the photon spectrum.

3.2. e-p Coulomb like heating

Here we investigate the effect of coulomb-type heating and we compare the results with those of Nayakshin & Melia (1998). We consider an unmagnetized source heated by a Coulomb-like process. We assume a closed system (no injection nor loss of particles) with a black body soft photon injection and we study its evolution under effect of Compton scattering, e-e Coulomb exchange, pair production/annihilation and a e-p Coulomb-like heating. The proton temperature characterizing the latter is set to 20 MeV. Two different cases are considered whose parameters are given in table 3. Whatever the initial distribution of parti-

	l_c	l_ν	$\tau_{e^-}^0$	Θ_ν
Model 1	420	420	0.05	10 ⁻⁴
Model 2	8.4	2.1	0.02	3 × 10 ⁻⁵

Table 3. Input parameters for the runs on the study of the e-p Coulomb like heating. $\tau_{e^-}^0$ is the initial electron Thomson optical depth. $\Theta_\nu = k_B T / m_e c^2$ is the temperature of the black body used for soft photons injection.

cles is, it always evolves to the same steady solution. The thermalization time however depends upon the exact initial

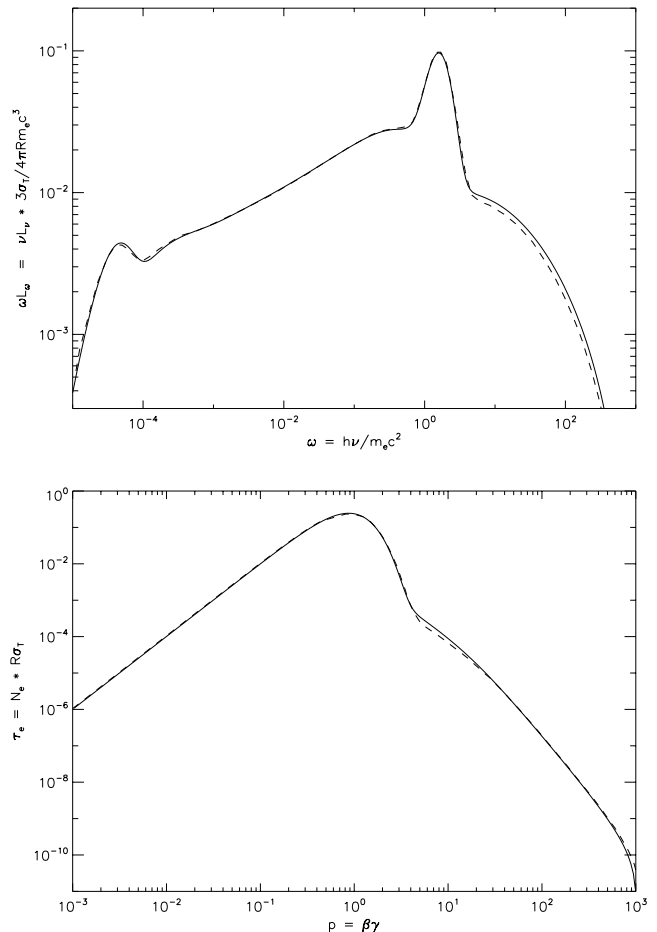


Fig. 2. Photons spectrum (upper panel) and particle distribution (lower panel) for power-law particle injection (with $l_e = 1$, $\gamma_{\min} = 1.4$, $\gamma_{\max} = 10^3$, $\Gamma = 2.4$) and for $l_\nu = 0.03$. The results with the code are shown in solid line and the results of Coppi (1992) are in dashed lines. Since the particle distribution at low energy in Coppi (1992) is assumed to be thermal but not exactly resolved, we extended it down to the grid boundary with a Maxwell distribution for comparison.

shape. Distributions in the transient phase can be found in Nayakshin & Melia (1998). We find similar results. Fig. 3 shows the steady distributions and spectra for the two cases and compares them to previous work. The steady states correspond to quasi-thermal distributions. Both the e-e Coulomb exchange and the e-p Coulomb-like interactions thermalize the plasma efficiently. In addition the e-p Coulomb-like interactions heat the particle distribution.

Our steady spectra are fully consistent with previous results: the Compton orders have the same amplitude and the high energy spectrum breaks at the same energy. Some output parameters are also given in table 4. Our results confirm qualitatively the results by Nayakshin & Melia (1998). The steady distributions have properties similar to those of a Maxwell-Boltzmann distribution but are narrower. Our results give however systematically hotter distributions and a larger optical depth in the most energetic case (model 2).

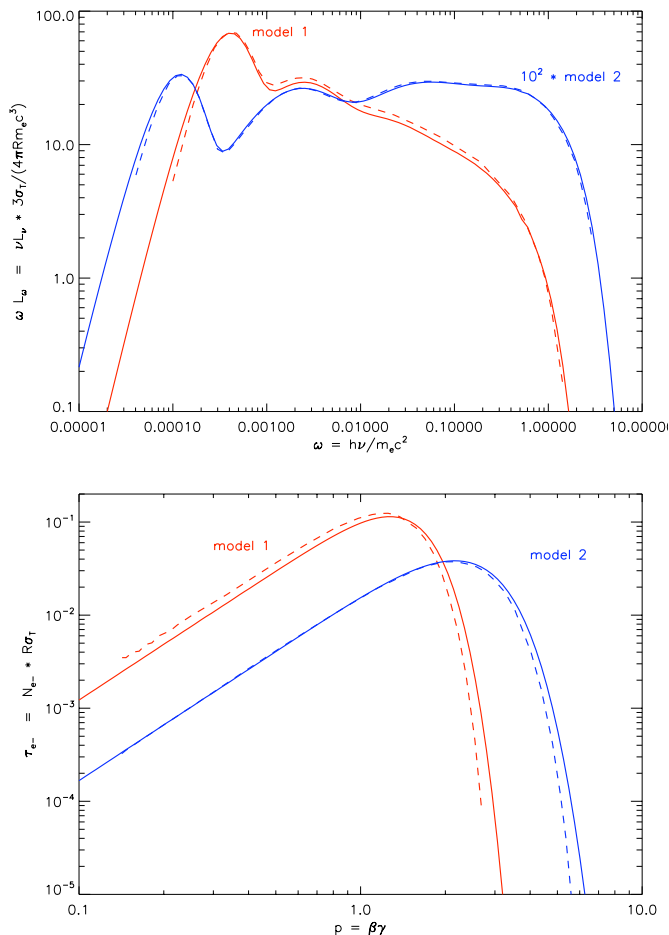


Fig. 3. Steady spectra (upper panel) and electron distribution (lower panel) for e-p Coulomb like heating. Solid and dashed lines show the results of this work and Nayakshin & Melia (1998) respectively. Inputs and outputs parameters are listed in tables 3 and 4 respectively.

Model	work	τ_{e-}	τ_{e+}	$\langle E_c \rangle$	η_3
1	NM98	0.135	0.085	0.58	2.4
	This work	0.132	0.082	0.65	110
2	NM98	0.080	0.060	1.46	0.44
	This work	0.086	0.066	1.53	17

Table 4. Output parameters. $\tau_{e\pm}$ are the electron and positron Thomson optical depths. $\langle E_c \rangle = \int (\gamma - 1) N_e dp / \int N_e dp$ is the averaged kinetic energy of the electron distribution. $\eta = \eta_3 \times 10^3$ is the heating efficiency defined by Eq. 24.

The heating efficiency coefficient is quite large: $\eta \approx 10^4 - 10^5$. This emphasizes how inefficient e-p Coulomb collisions are in cases typical of Seyfert galaxies for example. When the Thomson optical depth is much smaller than unity, they should be several orders of magnitude more efficient to reach the required heating rate. The efficiency coefficients found in this work are one or two orders of magnitude larger than the ones found in Nayakshin & Melia (1998). Given the good agreement obtained for the shape and normalisation of the distributions and escaping spec-

tra, we believe the different efficiencies are the result of a typo in their paper. We further checked our e-p Coulomb heating rate against the results of Dermer et al. (1996) and also against simple analytic approximations and found an excellent agreement.

3.3. Models with synchrotron soft photons

Magnetized models have an additional source of soft photons that is the synchrotron emission from high energy particles. We investigate this case by studying generic cases of magnetized sources with no external source of soft photons and we compare the results with those presented in Fig. 4 of Coppi (1992). Particles are injected at high energy ($\gamma = 10^3$). Since they are charged, we assume they are trapped by the magnetic field and do not escape. The equilibrium is thus balanced by pair annihilation. A few synchrotron self-Compton spectra are shown in Fig. 4 and compared to previous work. Other output parameters are listed in table 5.

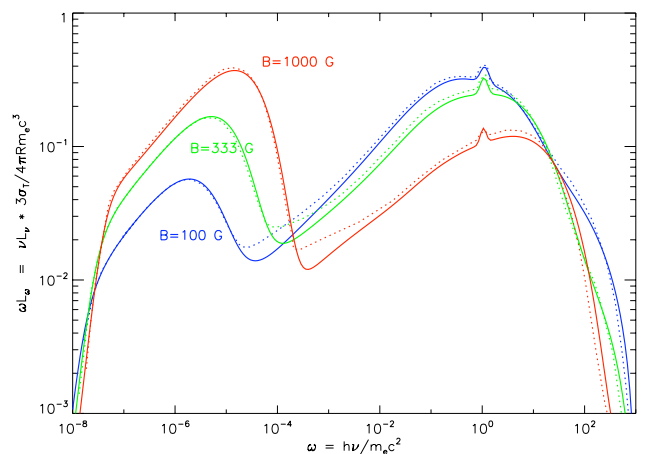


Fig. 4. Synchrotron self-Compton spectra. Spectra are shown with 3 magnetic field strengths ($l_B = 3.2 \times 10^{-2}, 3.2 \times 10^{-1}, 3.2$), from results of this work (solid lines) and of Coppi (1992) (dotted lines). Here, $l_e = 10$ and $R = 10^{14}$ cm.

B	work	PY ₃	τ_e	θ_3	l_X/l_e	α_{2-10}
100	Coppi92	21.0	0.508	37.3	82.4	0.578
	This work	18.9	0.513	64.1	72.6	0.561
300	Coppi92	15.4*	0.422	26.9*	58.6	0.609
	This work	13.5	0.434	44.7	49.4	0.604
1000	Coppi92	3.83	0.154	21.4	24.2	0.749
	This work	3.29	0.234	28.0	20.4	0.702

Table 5. Output parameters for synchrotron self-compton models. The magnetic field B is given in Gauss. Other parameters definitions are the same as in table 1. *Note that the pair yield and the temperature given by Coppi (1992) for B=300G have been multiplied by 10 to correct what we believe are typos.

Although the general spectrum shape is recovered, substantial difference can be observed in the far UV, soft X-ray band where the flux seems to have been underestimated in previous studies. We also get temperature for the thermal part of the distribution that are larger. This most likely results from our more precise treatment of the cyclotron emission/absorption.

3.4. The synchrotron boiler

Non thermal distributions of particles can be thermalized by the emission and absorption of synchrotron photons. The efficiency of this mechanism however depends on the parameters. To illustrate this process, we consider the case presented in Ghisellini et al. (1998a) where high energy particles strongly emit and absorb synchrotron photons. We inject a constant mono-energetic distribution of electrons into an empty source of size $R = 10^{13}$ cm. Electrons escape freely, which leads to a steady state. Here only cyclo-synchrotron radiation and Compton scattering are taken into account (pair effects, Coulomb scattering, and e-p Bremsstrahlung are turned off). Fig. 5 shows the time evolution of the particle and photon distributions and a comparison with previous work.

The results qualitatively confirm those of Ghisellini et al. (1998a). As time evolves, high energy particles are cooled down by the synchrotron radiation, which starts building the radiation field. Soft synchrotron photons are scattered up by high energy electrons and form the high energy part of the spectrum. With the choice of parameters ($l_{e^-}/l_B \ll 1$), the effect of synchrotron self-absorbed radiation on the particle distribution is dominant over Compton scattering so that the additional cooling on particles by the latter is negligible. The synchrotron cooling time scale for particle is then $t_s/(R/c) = (\gamma - 1)/(4l_B p^2/3) \approx 1/(\gamma + 1)/l_B$ and ranges between $0.5/l_B$ for low energy particles and $0.05/l_B$ for high energy particles ($\gamma \approx 20$). For $l_B = 10$, the distribution has reached a quasi-thermal shape at $t \approx 0.01 - 0.1R/c$, i.e. on the synchrotron time scale (see fig. 5). The normalization then saturates as the escape of particles balances the injection rate, which occurs on a typical time scale of $t_{esc} \gtrsim R/c$. The low energy part of the distribution matches a Maxwell distribution well but the high energy part of the distribution drops faster than a real thermal distribution. More precisely, the results are however different. For seek of clarity, the results of Ghisellini et al. (1998a) have not been over plotted but their distributions are systematically colder and broader than the previous ones, especially in the transient phase. In that respect, although the low energy part still looks thermal, the deviation at high energy is larger.

To illustrate the effect of the magnetic field intensity and the particle injection rate, we plot on Fig. 6 the temperature⁷ of the steady distribution as a function of the injection compactness parameter for 3 different magnetic compactness parameters. The steady temperature is rather insensitive to the magnetic parameter since it varies only by a factor less than 3 as l_B varies over more than 2 orders of magnitude. On the contrary, it is quite dependent on the injection compactness parameter. For a given magnetic field, the very low injection rates lead to steady states where the

⁷ the temperature is the effective temperature defined by Eq. (18) in Ghisellini et al. (1998a)

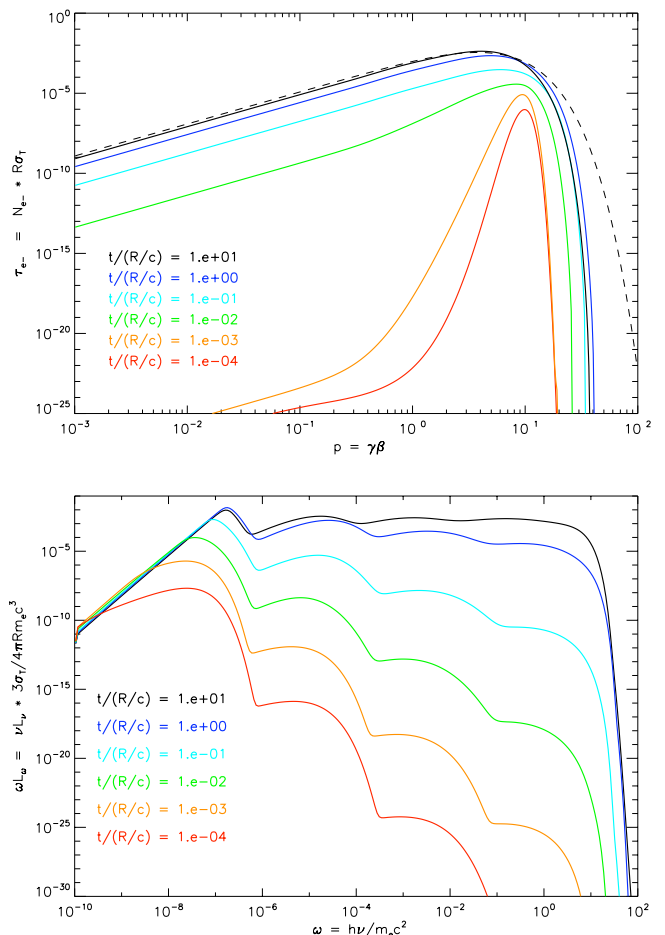


Fig. 5. Evolution of the particle distribution (upper panel) and the outgoing photon flux (lower panel). Times are $t/(R/c) = 10^{-4}, 10^{-3}, 10^{-2}, 10^{-1}, 1$ and 10 from lower to higher curves. Particles are injected with a Gaussian distribution centered at $\gamma = 10$, of width $\delta\gamma = 1$, and with a compactness parameter: $l_{e^-} = 1$. The magnetic compactness is $l_B = 10$ and the domain size is: $R = 10^{13}$ cm. The dashed curve is the Maxwell-Boltzmann distribution of same normalization and same average energy as the equilibrium solution.

Thomson optical depth is very low. The Compton cooling is negligible and the final temperature is large. As the injection parameter increases, the optical depth becomes large, the Compton cooling becomes efficient and dominates at high energy, which eventually leads to much smaller temperatures. The injection of particles at an energy much larger than the average one leads to the formation of a hard non-thermal tail and a larger deviation from the Maxwell distribution at high energies. Compared to the results by Ghisellini et al. (1998a), we find temperatures that are significantly higher (up to a factor 3) at large optical depths. This probably results from a more precise treatment of the radiation field and the Compton scattering. Ghisellini et al. (1998a) only considered the cooling of particles by inverse Compton scattering and assumed it is limited in the Thomson regime. By using the exact Klein-Nishina cross section we find faster photon escape and a smaller radiation field whose cooling efficiency is weaker.

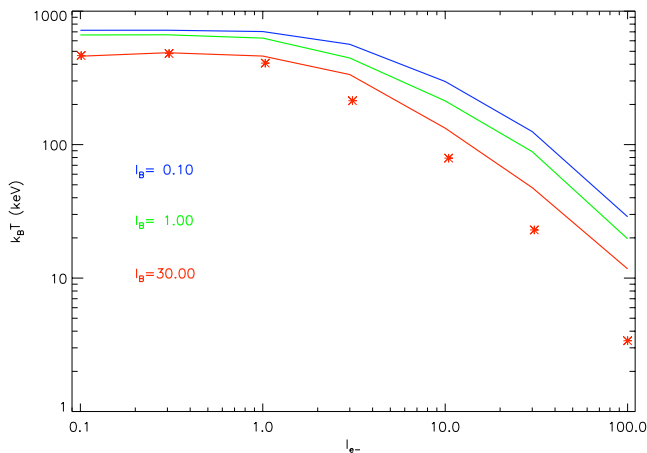


Fig. 6. Effective electrons temperature estimated following Eq. (18) in Ghisellini et al. (1998a). The 3 curves are for magnetic compactness parameters $l_B = 0.1, 1, 30$ from the higher to the lower respectively and the domain size is $R = 10^{13}$ cm. The stars show the results of Ghisellini et al. (1998a) for $l_B = 30$.

At large Thomson optical depth (i.e. at large injection rate), Coulomb exchange is supposed to become dominant over synchrotron self-absorption. To investigate this, we have done the same simulations including e-e Coulomb scattering. Results are shown on Fig. 7. It is found that the e-e

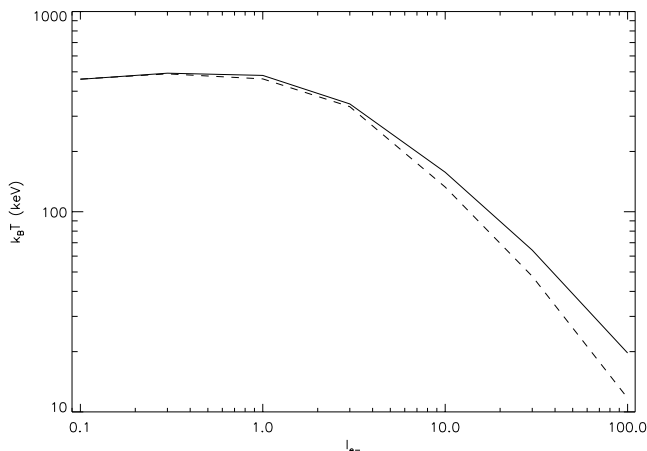


Fig. 7. Effect of Coulomb cooling: same as Fig. 6 for $l_B = 30$, with and without e-e Coulomb scattering (solid and dashed line respectively).

Coulomb collisions tend to increase the effective temperature. As explained before, particles are injected at high energy. They are cooled by both synchrotron emission and Compton scattering and form a low energy thermal pool. Then high energy particles scatter off thermal electrons by e-e Coulomb collisions. The cooling of the high energy distribution is very efficient but the thermal pool of cool electrons gain energy by this interaction, giving higher effective temperatures. This effect is negligible at low injection rate

when the temperature is so high that the injection energy almost lies in the bulk of the distribution and when there is no well-marked high energy tail. However, at large injection rate, the temperature becomes smaller so that particles are injected at much higher energies than that of the thermal pool. Exchange of energy between high energy and low energy particles becomes very efficient and it is found that this effect is significant (up to a factor 2 for $l_e = 100$).

A more detailed study of the synchrotron boiler mechanism and its application to X-ray binaries will be addressed in a future work.

3.5. Particle acceleration

As a second example we investigate the effect of Fermi 2nd order acceleration. We consider a magnetized ($l_B = 1$), isolated plasma of size $R = 5 \times 10^7$ cm (typical for X-ray binaries corona), with no injection of seed photons. The soft photons are emitted by synchrotron radiation of high energy particles. The acceleration is modeled by the second order Fermi process and no particle is injected into the plasma. Particles are assumed to be trapped and the Thomson optical depth is set to $\tau_e = 1$. Pair production/annihilation and Coulomb collisions are turned off to focus on the role of particle acceleration. After a transient phase that depends on the initial conditions, particles and photons reach a steady state that only depends on the acceleration properties.

We first investigate the role of the acceleration efficiency and the threshold energy is assumed to be much lower than the bulk of particles. Fig. 8 presents the steady particle distributions and spectra for various values of the acceleration efficiency. In all cases the distribution is very similar to a Maxwell-Boltzmann distribution. As was found in previous calculations the diffusion in the momentum space results in a quasi-thermal distribution (e.g. Katarzyński et al. 2006b) and in this case, the thermalization is helped by the synchrotron boiler mechanism. The spectrum is the sum of the low energy synchrotron emission and a hard tail resulting from the multiple Compton scatterings of these soft photons off the highest energy particles. As the acceleration efficiency increases the steady distribution widens and moves to higher energies. As a consequence, the spectra exhibit a stronger hard tail. The temperature of the distribution is given in table 6. As expected, it grows as the acceleration ef-

$\log(l_{\text{acc}})$	\bar{t}_{acc}	θ_3
-4	48800	164.5
-1	75.1	259.8
1	1.02	369.0
2	0.104	390.5

Table 6. Outputs parameters for Fig. 8. \bar{t}_{acc} is the acceleration time in unit R/c and θ_3 is the averaged temperature estimated as in section 3.1 in units of $10^{-3} m_e c^2$.

iciency increases. As there are more high energy particles the synchrotron self-absorbed emission is stronger, which cools down softer particles more efficiently and the averaged temperature saturates. The source luminosity however scales with the acceleration compactness parameter.

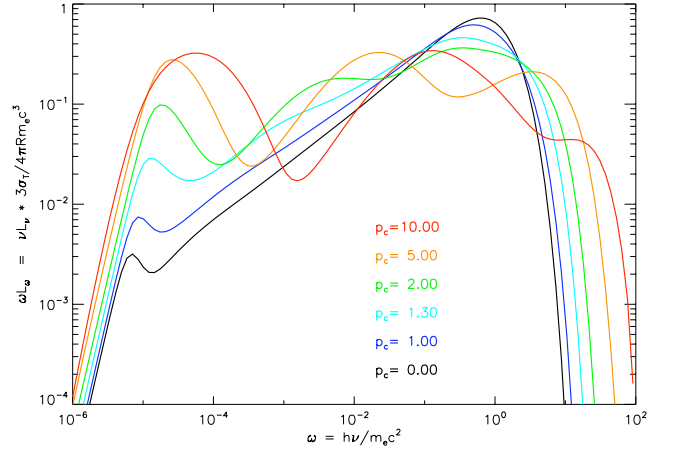
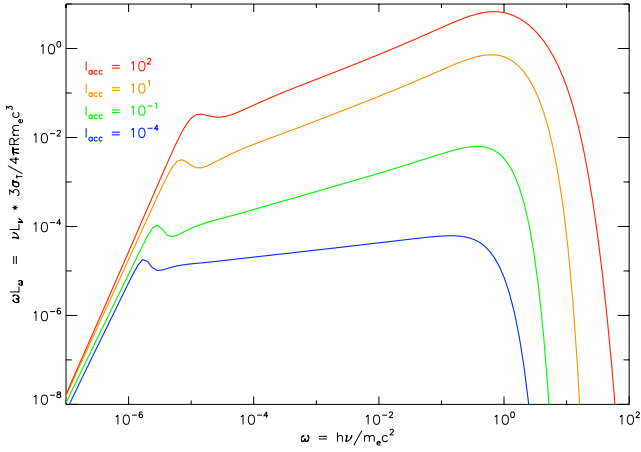
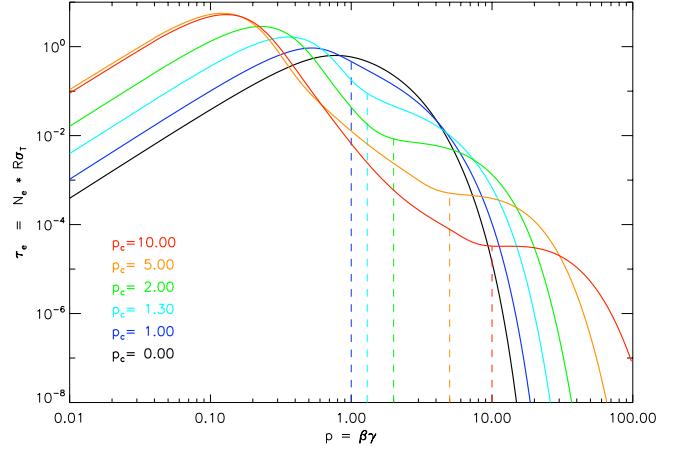
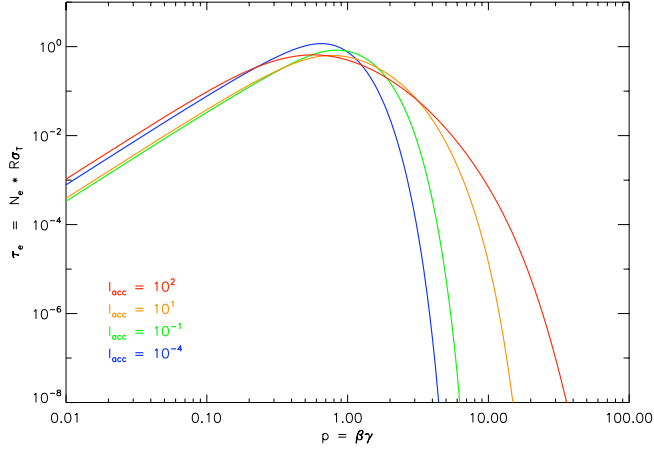


Fig. 8. Particle distributions (upper panel) and spectra (lower panel) for different acceleration efficiencies. Acceleration is modeled by second order Fermi process with no threshold. The optical depth is $\tau_e = 1$, the domain size is $R = 5 \times 10^7$ cm and the magnetic compactness parameter is $l_B = 1$.

We now investigate the role of the minimal energy above which the acceleration takes place. The simulations are run with the same parameters but the acceleration efficiency is set to $l_{acc} = 10$ and we vary the threshold energy. Note that for a given power supplied to the plasma by accelerating particles, the larger the threshold energy the fewer accelerated particles and the shorter their acceleration time. The results are shown in Fig. 9 for threshold momenta $p_c = 0, 1, 1.3, 2, 5$ and 10 . The corresponding acceleration times are $t_{acc} = 1.02, 6.32 \times 10^{-1}, 3.45 \times 10^{-1}, 1.77 \times 10^{-1}, 5.63 \times 10^{-2}, 1.95 \times 10^{-2} R/c$ respectively. For small threshold energies ($p_c \leq 1$), the distribution depends hardly on the exact threshold. It produces a small number of soft photons. Since the particles are not very energetic, the photons undergo multiple Compton scatterings and they form the strong high energy part of the spectrum. When only mid-relativistic or relativistic particles are accelerated, they form a high energy tail that extend far beyond the thermal pool and the situation is then very different. As the total synchrotron emission increases with the energy of the emitting particles ($\int j_s d\nu \propto p^2$) the synchrotron bump is much larger. Also, the hard energy tail of the particle distribu-

Fig. 9. Particle distributions (upper panel) and spectra (lower panel) for different threshold energies. Acceleration is modeled by second order Fermi process with $l_{acc} = 10$. The optical depth is $\tau_e = 1$, the domain size is $R = 5 \times 10^7$ cm and the magnetic compactness parameter is $l_B = 1$. Dashed vertical lines show the threshold momenta.

tion has a flat slope which produces a wider synchrotron bump. As the particles have higher energy, the Compton up scattering of these soft photons becomes more efficient. In this limit where the synchrotron soft photons have very low energy ($\omega_{synch} \ll 1$) and the accelerated electrons have high energy ($\gamma \gg 1$), the photon energy gain during one single scattering is: $\omega_{compt}/\omega_{synch} \approx 4\gamma^2/3$. As a result, photons undergo only a small number of Compton scatterings before they reach the particle energy, forming a double humped spectrum as those of blazars in the case $p_c = 10$. In the same time, Compton scattering cools down the thermal particles further so that the bulk of particles moves to lower energies. Future work will consider in more details this effect including the physics of wave-particle interaction. In particular more consistent models of particle escape and momentum diffusion have to be implemented.

Conclusion

We have presented a code developed to deal with radiation processes in high energy plasmas with no approximation on the shape of the particle distribution. The code

is time dependent. It deals with the exact Compton and pair production/annihilation unpolarized, isotropic cross sections. Cyclo-synchrotron self-absorbed radiation is taken into account from the sub-relativistic regime to the ultra-relativistic one, which represent an improvement compared to other codes. It also includes an approximate treatment of e-e and e-p Coulomb exchange and of e-p self-absorbed Bremsstrahlung radiation. Last, explicit prescriptions for particle acceleration have been implemented. The code consistently deals with all these processes over very large ranges of energy: there is no restriction on the photon energy and allows for particles from $\gamma - 1 \gtrsim 10^{-14}$ to $\gamma \lesssim 10^7$. Therefore it can be used to model a large number of different sources such as X-ray binaries and AGN but also γ -ray bursts or pulsar wind nebulae.

The major limitation of the code is the lack of explicit treatment of the geometry. The code simulates a uniform system, typically an homogeneous sphere with an isotropic and unpolarized radiation field. It obviously introduces a bias in simulations of X-ray binaries coronae where the seed photons from the disk are not isotropic or in jets of AGN where geometrical effects are important. However, the geometry of the emitting regions in high energy sources is not constrained and in most cases it does not play a crucial role. Moreover, the prescriptions used for particle and photon escape can to some extent reproduce the main effects of geometry.

Some examples were shown in this paper to check the code capabilities against previous codes that have been designed to solve restricted problems, involving a limited number of ingredients. In several cases we have disabled some processes in our code to make more rigorous comparisons. We have found that the code confirms qualitatively all previous results. As we deal more precisely with some processes, the properties of the exact spectra and particle distribution are however slightly different. As a new example, we investigated the acceleration by second order Fermi-like processes. We find that an energy threshold for acceleration leads to the formation of a non-thermal population of particles when it reaches the mid-relativistic regime.

References

- Alexanian, M. 1968, *Physical Review*, 165, 253
 Belmont, R., *A&A*, 2008, submitted to *A&A*
 Bisnovatyi-Kogan, G. S., Zel'Dovich, Y. B., & Syunyaev, R. A. 1971, *Soviet Astronomy*, 15, 17
 Blasi, P. 2000, *ApJ*, 532, L9
 Brinkmann, W. 1984, *Journal of Quantitative Spectroscopy and Radiative Transfer*, 31, 417
 Boettcher, M. & Schlickeiser R., 1997
 Böttcher, M., & Liang, E. P. 2001, *ApJ*, 552, 248
 Chang, J. S., & Cooper, G. 1970, *Journal of Computational Physics*, 6, 1
 Coppi, P. S. 1992, *MNRAS*, 258, 657
 R. Courant, K. Friedrichs & Lewy, H. 1967, *IBM Journal*, 215, English translation of the 1928 German original
 Crusius, A., & Schlickeiser, R. 1986, *A&A*, 164, L16
 Dermer, C. D., & Liang, E. P. 1989, *ApJ*, 339, 512
 Dermer, C. D., Miller, J. A., & Li, H. 1996, *ApJ*, 456, 106
 Fabian, A. C., Guilbert, P. W., Blandford, R. D., Phinney, E. S., & Cuellar, L. 1986, *MNRAS*, 221, 931
 Ghisellini, G. 1987, *MNRAS*, 224, 1
 Ghisellini, G., Guilbert, P. W., & Svensson, R. 1988, *ApJ*, 334, L5
 Ghisellini, G., & Svensson, R. 1991, *MNRAS*, 252, 313
 Ghisellini, G., Haardt, F., & Fabian, A. C. 1993, *MNRAS*, 263, L9
 Ghisellini, G., Haardt, F., & Svensson, R. 1998, *MNRAS*, 297, 348
 Ghisellini, G., Celotti, A., Fossati, G., Maraschi, L., & Comastri, A. 1998, *MNRAS*, 301, 451
 Gorecki, A., & Wilczewski, W. 1984, *Acta Astronomica*, 34, 141
 Gould, R. J. 1980, *ApJ*, 238, 1026
 Guilbert, P. W. 1981, *MNRAS*, 197, 451
 Guilbert, P. W., & Stepney, S. 1985, *MNRAS*, 212, 523
 Guilbert, P. W. 1986, *MNRAS*, 218, 171
 Haug, E. 1975, *Zeitschrift Naturforschung Teil A*, 30, 1099
 Haug, E. 1985, *Phys. Rev. D*, 31, 2120
 Heitler, W. 1954, *International Series of Monographs on Physics*, Oxford: Clarendon, 1954, 3rd ed.
 Jauch, J. M., & Rohrlich, F. 1976, *Texts and Monographs in Physics*, New York: Springer, 1976, 2nd ed.
 Jones, F. C. 1968, *Physical Review*, 167, 1159
 Katarzyński, K., Ghisellini, G., Svensson, R., & Gracia, J. 2006, *A&A*, 451, 739
 Katarzyński, K., Ghisellini, G., Mastichiadis, A., Tavecchio, F., & Maraschi, L. 2006, *A&A*, 453, 47
 Kusunose, M. 1987, *ApJ*, 321, 186
 Le Roux, E. 1960, *Annales d'Astrophysique*, 23, 1010
 Li, H., Kusunose, M., & Liang, E. P. 1996, *ApJ*, 460, L29
 Li, H., & Miller, J. A. 1997, *ApJ*, 478, L67
 Lightman, A. P., Zdziarski, A. A., & Rees, M. J. 1987, *ApJ*, 315, L113
 Lightman, A. P., & Zdziarski, A. A. 1987, *ApJ*, 319, 643
 Le Roux, E. 1961, *Annales d'Astrophysique*, 24, 71
 McCray, R. 1969, *ApJ*, 156, 329
 Malzac, J., & Jourdain, E. 2000, *A&A*, 359, 843
 Marcowith, A., & Malzac, J. 2003, *A&A*, 409, 9
 Nagirner, D. I., & Poutanen, J. 1994, *Single Compton scattering, Astrophysics and Space Physics Reviews*, vol. 9, part 1. Amsterdam: Harwood Academic Publishers, c1994, 83 pages.,
 Nayakshin, S., & Melia, F. 1998, *ApJS*, 114, 269
 Park, B. T., & Petrosian, V. 1996, *ApJS*, 103, 255
 Pe'er, A., & Waxman, E. 2005, *ApJ*, 628, 857
 Poutanen, J., & Svensson, R. 1996, *ApJ*, 470, 249
 Pozdnyakov, L. A., Sobol, I. M., & Siuniaev, R. A. 1977, *Soviet Astronomy*, 21, 708
 Pozdnyakov, L. A., Sobol, I. M., & Syunyaev, R. A. 1980, *Comptonization and radiation spectra of X-ray sources. Calculation of the Monte Carlo method*, Rept. Pr-447 Acad. of Sci. USSR, Moscow, 1978 12 p,
 Pozdnyakov, L. A., Sobol, I. M., & Siuniaev, R. A. 1983, *Astrophysics and Space Physics Reviews*, 2, 189
 Stepney, S. 1983, *MNRAS*, 202, 467
 Stepney, S., & Guilbert, P. W. 1983, *MNRAS*, 204, 1269
 Stern, B. E., Begelman, M. C., Sikora, M., & Svensson, R. 1995, *MNRAS*, 272, 291
 Sunyaev, R. A., & Titarchuk, L. G. 1980, *A&A*, 86, 121
 Svensson, R. 1982, *ApJ*, 258, 321
 Svensson, R. 1982, *ApJ*, 258, 335
 Svensson, R. 1983, *ApJ*, 270, 300
 Svensson, R. 1984, *MNRAS*, 209, 175
 Svensson, R. 1987, *MNRAS*, 227, 403
 Wardziński, G., & Zdziarski, A. A. 2000, *MNRAS*, 314, 183
 Zdziarski, A. A. 1984, *ApJ*, 283, 842
 Zdziarski, A. A. 1985, *ApJ*, 289, 514
 Zdziarski, A. A., Lightman, A. P., & Maciolek-Niedzwiecki, A. 1993, *ApJ*, 414, L93